EFFECT OF FLUID DYNAMICS CONDITIONS AND COMBUSTION REACTIONS ON THE PERFORMANCE AND HEAT AND MASS TRANSFER DISTRIBUTION OF DUAL-PHASE OXYGEN TRANSPORT MEMBRANES

by

Wei BAI[a*], Jun-Xiao FENG[a], Huan-Bao FAN[a], and Yu-Jie ZHAO[b]

[a] School of Energy and Environmental Engineering,
University of Science and Technology Beijing, Beijing, China
[b] School of Mechanical Engineering, Changzhou University, Changzhou, Jiangsu, China

Original scientific paper
https://doi.org/10.2298/TSCI220625199B

A 3-D model based on CFD approach was developed to explore the effect of fluid dynamic conditions and combustion reactions on oxygen transport, in which the distribution of parameters such as oxygen partial pressure, temperature, velocity, and oxygen permeability were considered. After meshing the geometric model with poly-hexcore method, a series of user defined functions written in C++ were compiled and hooked to FLUENT to solve for oxygen permeation of dual-phase oxygen transport membranes. The results showed that oxygen permeability can be improved by pressurizing the feed side or vacuuming the permeate side, and the increased kinetic effect under evacuation conditions can increase the oxygen permeability by 69.85% at a vacuum pressure of 10 kPa and by 270.94% at 90 kPa. Due to the phenomenon of differential concentration polarization, the effect of oxygen concentration on oxygen permeability is more significant when the oxygen concentration on the feed side is lower than 0.17. Combustion reaction of CH_4 promotes oxygen permeation, and the effect of the gap height between the fuel inlet and membrane is determined by several trade-off factors including momentum effects, reaction rate and temperature, and optimal oxygen permeability is achieved with a gap height of 3 mm.

Key words*: oxygen transport membranes, CFD, fluorite, perovskite*

Introduction

Inorganic dense ceramic-based oxygen transport membranes (OTM) with the advantages of low cost and high oxygen purity have attracted attention because of their applications in solid oxide fuel cells and catalysts and the production of pure oxygen for many large-scale industrial processes, such as CO_2 capture, coal gasification, oxygen-enriched combustion, and natural gas conversion syngas *etc*. [1-7]. Furthermore, it is possible to integrate oxygen separation and a catalytic reaction in a single reactor [8-10].

Single-phase OTM such as $Ba_{0.5}Sr_{0.5}Co_{0.8}Fe_{0.2}O_{3-\delta}$ [11] and $La_{0.6}Sr_{0.4}Co_{0.2}Fe_{0.8}O_{3-\delta}$ [12] have been widely studied for their excellent oxygen permeability. Unfortunately, the weak stability limits the industrialization of single-phase membranes. In recent years, dual-phase OTM such as $C_{e0.85}Sm_{0.15}O_{2-\delta}$-$Sm_{0.6}Sr_{0.4}Al_{0.3}Fe_{0.7}O_{3-\delta}$ (SDC-SSAF) [13] have demonstrated greater stability in harsh environments by reducing the harsh requirements for a single material. In addition the influence of material properties on OTM, the operation parameters are also crucial

* Corresponding author, e-mail: mr_white686@163.com

[14]. Specially, the oxygen permeation process is based on the local conditions near the membrane surface [15]. Therefore, it is very important to understand the internal flow field, oxygen concentration and temperature distribution during its working process to further analyze the oxygen permeation mechanism and improve the oxygen permeability [3, 16]. The commonly used experimental methods are not only expensive and time-consuming, but also difficult to operate the specific distribution of important parameters in real-time intuitive feedback process [17]. The CFD is an effective tool to simulate local fluid changes and heat and mass transfer characteristics in membrane modules [18]. There are few CFD simulations of oxygen permeation processes, and only a few reports on the simulation of conventional single-phase membrane materials have been reviewed. For example, Habib's group [19] investigated the effect of adding CH_4 as sweep gas to the permeate side on the effect of oxygen permeation. Feng *et al.* [20] developed a 3-D hollow fiber membrane module model and considered the heat and mass transfer along the radial direction of the hollow fiber. However, the mechanism and oxygen permeation equation of dual-phase membranes are different from those of single-phase membranes. Therefore, CFD simulation analysis of dual-phase OTM is of great importance to fill the research gap in this direction and guide future industrial applications.

In this paper, taking SDC-SSAF as the research object, the effects of operating pressure, feed oxygen concentration and CH_4 combustion on the oxygen permeation process are investigated in terms of the distribution of velocity, oxygen partial pressure and temperature by constructing a 3-D oxygen permeation model. The oxygen separation process was effectively simulated by the user-defined function (UDF) of the oxygen permeation model written by VC^{++}, and compiled and connected in FLUENT19.0 software.

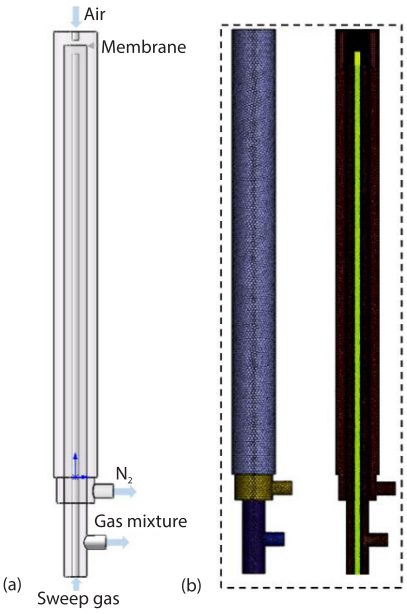

Figure 1. The geometric model and grid division of oxygen permeation

Modelling and methodology

The geometric model and mesh division

The geometric model was constructed as shown in fig. 1(a) based on the home-built performance test system. Since the mass-flow controller controls the gas to flow at a uniform velocity, the inlet near the membrane was used as the gas velocity inlet in the later simulation calculation. The geometric model was meshed by the poly-hexcore meshing method in the FLUENT Meshing software, and the inlet and outlet, the fluid boundary, and the membrane vicinity were locally refined to improve the simulation calculation accuracy, as shown in fig. 1 (b).

Governing equation

The governing equations include mass, momentum and energy conservation equations. The mass-flow through the membrane can be obtained by the equation containing the source/sink term. At the membrane boundary, oxygen species disappear at the feed side through the sink term and form at the permeate side through the source term [20-25]:

$$\frac{\partial}{\partial x_j}\rho U_j = S_i \tag{1}$$

$$\frac{\partial}{\partial x_j}\left(\rho U_i U_j\right) = -\frac{\partial}{\partial x_i}p + \mu\frac{\partial^2}{\partial x^2}U_j \tag{2}$$

$$\left(\rho C_p\right)_f U_i \frac{\partial}{\partial x_j}T = \frac{\partial}{\partial x_j}k_f \frac{\partial}{\partial x_j}T + S_h \tag{3}$$

$$\frac{\partial}{\partial x_j}\left(\rho U_j Y_i\right) - \frac{\partial}{\partial x_i}\rho D_{i,m}\frac{\partial}{\partial x_j}Y_i = S_i \tag{4}$$

The diffusion coefficients of the components are determined:

$$D_{i,m} = \frac{1 - X_i}{\sum_{j,j\neq i}\left(\frac{X_i}{D_{i,j}}\right)} \tag{5}$$

The oxygen flux transported through the oxygen permeable membrane is calculated according to the source term equation:

$$S_i = \begin{cases} +\dfrac{J_{\mathrm{O}_2} A_{\mathrm{cell}}}{V_{\mathrm{cell}}} & \text{Penetration side} \\ -\dfrac{J_{\mathrm{O}_2} A_{\mathrm{cell}}}{V_{\mathrm{cell}}} & \text{Feed side} \end{cases} \tag{6}$$

The radiation heat transfer equation of discrete co-ordinate model:

$$\nabla\left[I(\vec{\mathrm{r}},\vec{\mathrm{s}})\vec{\mathrm{s}} + \left(a+\sigma_s\right)I(\vec{\mathrm{r}},\vec{\mathrm{s}})\right] = an^2\frac{\sigma T^4}{\pi} + \frac{\sigma_s}{4\pi}\int_0^{4\pi}(\vec{\mathrm{r}},\vec{\mathrm{s}})\,j(\vec{\mathrm{s}}\times\vec{\mathrm{s}})\mathrm{d}\Omega \tag{7}$$

The one-step finite rate reaction kinetics model of methane was used to construct the reaction kinetics model:

$$R_{\mathrm{CH}_4} = -k\left[\mathrm{CH}_4\right]^{n_{\mathrm{CH}_4}}\left[\mathrm{O}_2\right]^{n_{\mathrm{O}_2}} \tag{8}$$

where k is the Arrhenius reaction rate, the expression is:

$$k = AT^{\beta}\exp\left(\frac{-E_a}{\mathrm{R}T}\right) \tag{9}$$

Oxygen permeation model

Through the analysis of bulk and interface for membrane, the general transport equation is derived in eq. (10). The total chemical potential difference and total resistance through the membrane are shown [26, 27]:

$$J_{\mathrm{O}_2} = -\frac{\Delta\mu_{\mathrm{O}_2}^{\mathrm{tot}}}{4^2F^2}\frac{1}{r^{\mathrm{tot}}} \tag{10}$$

$$\Delta\mu_{\mathrm{O}_2}^{\mathrm{tot}} = \Delta\mu_{\mathrm{O}_2}' + \Delta\mu_{\mathrm{O}_2}^{b} + \Delta\mu''\mathrm{O}_2 = \mathrm{R}T\ln\frac{P_{\mathrm{O}_2}^{\mathrm{II}}}{P_{\mathrm{O}_2}^{\mathrm{I}}} \tag{11}$$

$$r^{\mathrm{tot}} = r' + r^{b} + r'' \tag{12}$$

The specific permeation resistance of each membrane interface can be obtained by eqs. (13) and (14), and constants r', r^b, and r'' at specific temperature can be obtained by substituting eqs. (13) and (14) into eq. (12) in turn and llinear regression:

$$r' = r'_o \left(\frac{P^{\mathrm{I}}_{\mathrm{O}_2}}{P_o} \right)^{-1/2} \tag{13}$$

$$r'' = r''_o \left(\frac{P^{\mathrm{II}}_{\mathrm{O}_2}}{P_o} \right)^{-1/2} \tag{14}$$

The oxygen permeation formula as shown in eq. (15) of dual-phase OTM can be obtained by combining eqs. (10)-(14):

$$J_{\mathrm{O}_2} = -\frac{\mathrm{R}T \ln \dfrac{P^{\mathrm{II}}_{\mathrm{O}_2}}{P^{\mathrm{I}}_{\mathrm{O}_2}}}{4^2 F^2} \frac{1}{r'_o \left(\dfrac{P^{\mathrm{I}}_{\mathrm{O}_2}}{P_o} \right)^{-1/2} + r^b + r''_o \left(\dfrac{P^{\mathrm{II}}_{\mathrm{O}_2}}{P_o} \right)^{-1/2}} \tag{15}$$

The permeation parameters between 800 °C and 950 °C can be obtained by linear regression of experimental data using eqs. (10)-(14), as shown in tab. 1.

Table 1. The regression oxygen permeation parameters of SDC-SSAF at 800-950 °C [28]

Temperature [°C]	r'_o [$10^2\Omega\mathrm{cm}^2$]	r''_o [$10^2\Omega\mathrm{cm}^2$]	r^b [$10^2\Omega\mathrm{cm}^2$]	R^2
950	10.58	1.22	43.33	0.9893
925	12.11	1.57	44.99	0.9988
900	14.64	1.61	53.06	0.9946
875	17.52	2.07	62.01	0.9910
850	27.24	2.35	62.66	0.9752
825	43.72	2.39	75.12	0.9685
800	68.63	2.44	94.84	0.9580

Results and discussion

Model verification

Figure 2 show the comparison between the experimental test data and simulated values of the changes of oxygen permeability of prepared SDC-SSAF membrane at 800-950 °C and velocity vector distribution plot. It can be seen that the experimental and simulated values basically agree with each other, and their error values are all within 8%, which proves that the constructed model can be used for calculation of SDC-SSAF dual-phase OTM. The error value fluctuation after 900 °C is mainly due to the error during the experimental test. The almost linear increase in oxygen permeability with increasing operating temperature is attributed to the increase in membrane surface exchange rate and oxygen diffusion rate through the oxygen membrane with increasing temperature. The velocity vector diagram visualizes the specific distribution of velocity magnitude and direction in the basin space. The air inlet exhibits a max-

imum velocity of 0.17 m/s. After the inlet gas on both sides hit the membrane, the velocity direction changes and flows at a lower velocity in the casing until it reaches the outlet, where the velocity increases due to the reduction of the flow area. It is worth noting that the fluid exhibits a certain expansion angle at the inlet, so the inlet diameter of the permeation side should not be chosen too large to avoid causing part of the sweep gas to hit the pipe wall and thus inhibit the sweep effect. Figure 3 show that the oxygen concentration distribution near the membranes on both sides shows a lamellar decreasing trend.The oxygen concentrations on both sides near the membrane are 0.2275 and 0.0269, respectively, and there is an accumulation of oxygen concentration at the peripheral corners of the permeate side. This is caused by the low flow rate in this region, which is precisely demonstrated in the velocity vector distribution diagram.

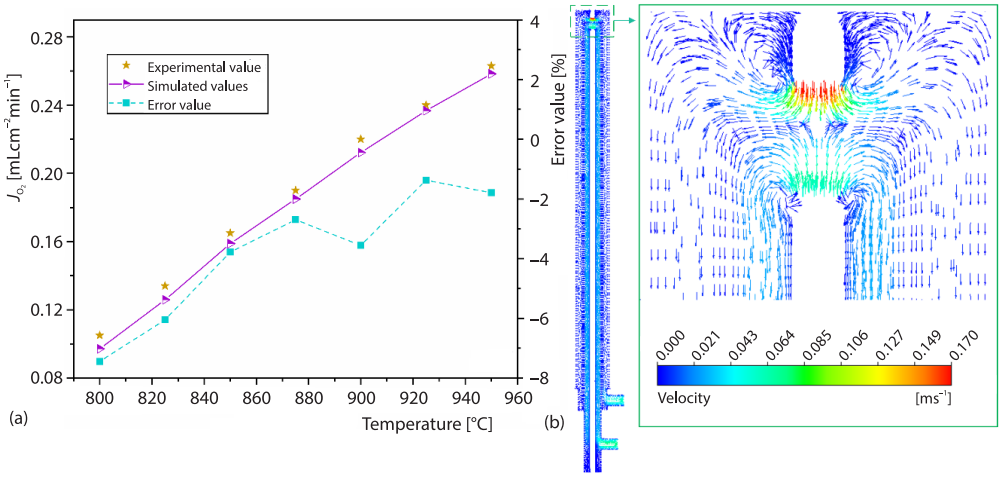

Figure 2. Comparison of experimental and simulated values of oxygen permeability at 800-950 °C (a) and velocity vector distribution plot (b)

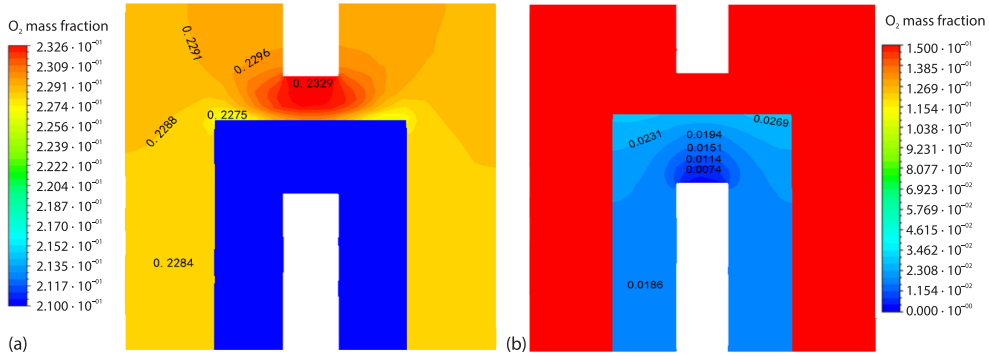

Figure 3. Oxygen concentration mass ratio on the feed side (a) and oxygen concentration mass ratio on the permeate side (b)

Effect of operating pressure

The oxygen permeation driving force comes from the oxygen partial pressure gradient on both sides of the membrane. In addition the effect of oxygen concentration, the oxygen partial pressure is also closely related to the basin space pressure. Therefore, pressurizing the air

feed side or evacuating the permeate side can achieve a change in the oxygen gradient and thus increase the oxygen permeation effect. Pressure values of 30 kPa, 60 kPa, 100 kPa, 150 kPa, and 200 kPa are applied to the feed side to achieve a change in the oxygen gradient. Figure 4 shows the variation of oxygen permeability with the pressurized value on the feed side at different heat source temperatures. It can be seen that there is a significant increase in oxygen permeability after pressure application compared to atmospheric pressure, with an increase of nearly two times at 800 °C. This is due to the positive correlation between oxygen permeability and oxygen partial pressure gradient, while the oxygen partial pressure on both sides is equal to the product of the pressure in the basin space and the corresponding oxygen concentration, which leads to an elevated oxygen partial pressure gradient when the pressure on the feed side increases. The pressure on the feed side decreases in a stepwise manner from the inlet to the outside before pressurization, and the pressure distribution cloud shows an overall increase in the basin space on the feed side after pressurization. When the pressurization value is within 200 kPa, the oxygen permeability shows a linear increase with the increase of pressurization value. The growth of oxygen permeability slows down after the pressurization value on the feed side exceeds 30 kPa. Feng *et al.* [20] in their study of $La_{0.6}Sr_{0.4}Co_{0.2}Fe_{0.8}O_{3-\delta}$ single-phase perovskite materials found that for the increase of the feed side space pressure from 0.5-5 MPa, the oxygen permeability showed a trend of increasing first and then changing smoothly, therefore, it is not wise to significantly increase the pressurization value on the feed side for the benefit of the oxygen permeation effect, which is not only a poor return on the cost paid in engineering applications, but also more difficult to achieve.

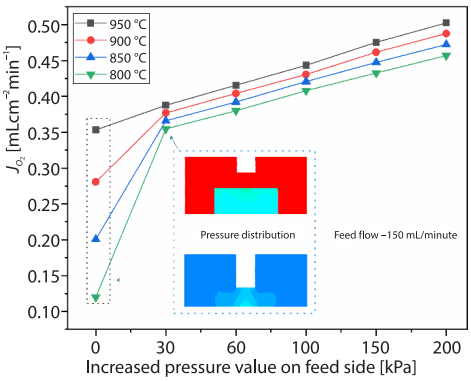

Figure 4. Variation of oxygen permeability with the value of pressurization on the feed side at different heat source temperatures (feed flow rate = S_{sweep} flow rate = 150 mL per minute)

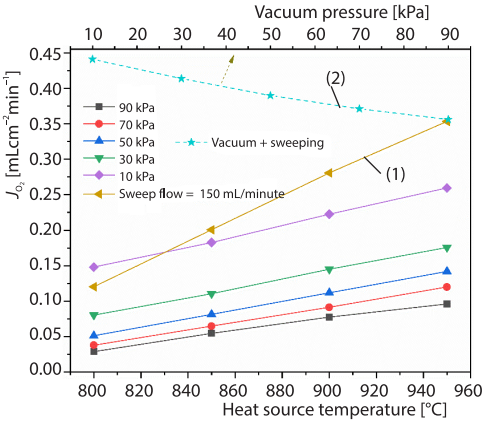

Figure 5. Comparison of the variation of oxygen permeability with temperature for different vacuum and sweep conditions (1) and the effect of sweep gas on oxygen permeation effect under vacuum conditions (2)

In this paper, the effect of permeate side vacuum on the oxygen permeation effect is studied in three aspects. The variation law of oxygen permeability with temperature under different vacuum pressures was firstly investigated. Then the effect of CO_2 sweeping with an inlet flow rate of 150 mL per minute was compared with the effect of evacuation conditions. Vacuuming the permeation space caused results similar to the dilution effect on the oxygen on the permeation side, and to verify this idea, the effect of increasing the sweeping conditions on the oxygen permeation effect at the vacuum level was finally analyzed. The results of the study

in fig. 5 show that, as expected, the oxygen partial pressure decreases as the vacuum pressure on the permeate side decreases, resulting in an enhanced oxygen permeation effect. The oxygen permeability under higher vacuum pressure is smaller than that under sweeping condition, and the oxygen permeation effect is comparable to that of sweeping condition when the vacuum pressure is 10 kPa. The oxygen permeability with increased sweep conditions is much higher at any vacuum pressure than that produced by evacuation alone at a heat source temperature of 950 °C. Taking the vacuum pressure of 10 kPa as an example, the oxygen permeability increased by 69.85% with the increase of sweeping conditions. This is mainly due to the kinetic effect of sweep gas, the collision and friction effect between sweep gas molecules and oxygen molecules accelerates the blowing away of oxygen molecules from the membrane surface, while relying only on the vacuum conditions is only equivalent to the dilution of oxygen, the absence of the external momentum of oxygen molecules leaving the membrane surface. Figure 6 shows the comparison of the oxygen permeability values under both sweeping and non-sweeping conditions at different vacuum pressures, and it can be found that with the increase of vacuum pressure, oxygen permeability also increases from 69.85-270.94% after increasing the sweeping condition. The reason is that the low vacuum level leads to insufficient dilution of oxygen, and the driving force of oxygen partial pressure gradient is difficult to meet the demand of oxygen penetration, when the increase of sweeping is more obvious for the blowing off of oxygen molecules [27].

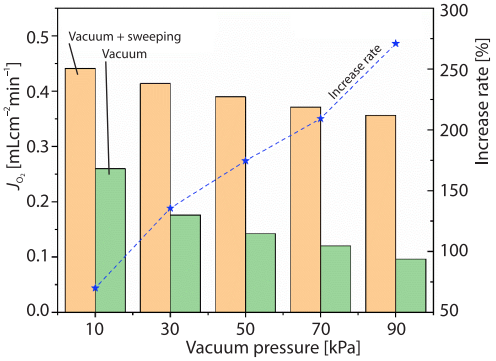

Figure 6. Comparison of the variation of oxygen permeation with vacuum pressure under both sweeping and non-sweeping conditions at different vacuum pressures

Effect of feed oxygen concentration

When the amount of oxygen provided on the feed side is difficult to meet the demand of O^{2-} bulk diffusion of the membrane, the phenomenon of concentration polarization occurs on the membrane surface of the feed side. In other words, under low feed flow rate, oxygen in air is driven by oxygen partial pressure through the membrane, and nitrogen is trapped in the feed side, thus the concentration gradually increases in the region, and under the effect of concentration gradient, nitrogen will diffuse backwards, which increases fluid resistance and local osmotic pressure. on the other hand, because the provided oxygen amount cannot meet the oxygen vacancy transmission, the oxygen depletion in the feed side makes the membrane surface local oxygen partial pressure decreases, which leads to the decrease of oxygen perme-

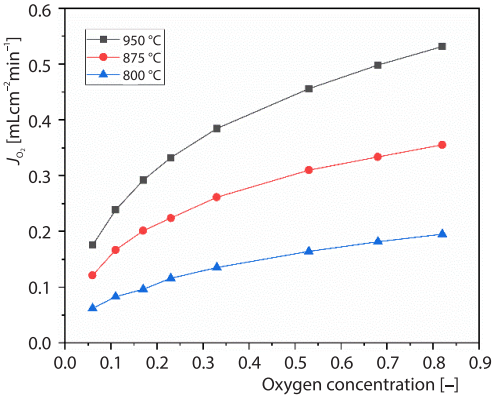

Figure 7. Trends in the effect of feed oxygen concentration on oxygen permeability at heat source temperatures of 800 °C, 875 °C, and 950 °C (feed side inlet flow rate of 150 mL per min^{ute} and purge flow rate of 100 mL per min^{ute})

ation effect [29]. The inlet air oxygen concentration directly determines the oxygen partial pressure on the feed side. At the same flow rate, a larger oxygen concentration can increase the oxygen partial pressure gradient, so that the limit value of the feed flow rate affected by the concentration difference polarization resistance is reduced [30]. Figure 7 shows the trend of the effect of feed concentration on the oxygen permeation effect at heat source temperatures of 800 °C, 875 °C, and 950 °C. When the oxygen concentration increased from 0.06-0.82, the oxygen permeability increased from 0.062, 0.121, and 0.175 mL/cm^{2}min to 0.195, 0.355, and 0.531 mL/cm^{2}min at the three temperatures of 800 °C, 875 °C, and 950 °C, the growth values were 0.133, 0.234, and 0.356 mL/cm^{2}min, respectively, and the growth rate was positively correlated with temperature. It can be seen that simply increasing the oxygen partial pressure gradient is not ideal for improving oxygen permeation because the membrane has a low surface exchange rate and diffusion rate when working at low temperatures. When the oxygen concentration ratio is lower than 0.17, the change of oxygen permeability is relatively obvious, and the reason is still affected by the resistance of concentration polarization.

Effect of CH_4 combustion

The introduction of CH_4 cannot only solve the high separation cost caused by inert gas sweeping, but also eliminate the additional condensation process associated with water vapor sweeping. This section explores the effect of CH_4 combustion on the oxygen permeation process. Figure 8 shows the comparison of the change law of oxygen permeability and its increase rate under reactive and non-reactive conditions. in the heat source temperature range of 800-950 °C, and oxygen permeability increased by 190.92% at 800 °C. The introduction of the combustion reaction resulted in improved oxygen permeability at all temperatures compared to the CO_2-only flow sweeping condition. This is due to the fact that the high temperature zone of the flame generated by the combustion increases the actual working temperature of the membrane, and the permeation process occurs under non-isothermal conditions [31]. On the other hand, as previously stated, the flow sweeping of inert gas always results in the formation of high oxygen concentration in the peripheral corner area of the permeate side, which reduces the driving force of oxygen permeation, and the combustion of CH_4 just consumes this part of oxygen. Under the reaction condition, the increase of oxygen permeability with temperature is small, and the increase rate of oxygen permeability relative to the flow sweeping condition decreases with the increase of temperature, that is, the promotion effect of combustion reaction on oxygen permeability is weakened at high temperature. This is because the temperature source of the membrane at this time is not only the heat source temperature, but also the suspended flame generated by combustion, which makes the OTM ensure a relatively high working temperature in time at low heat source temperature, and the high temperature generated by combustion becomes the dominant factor controlling the working temperature of the membrane [32].

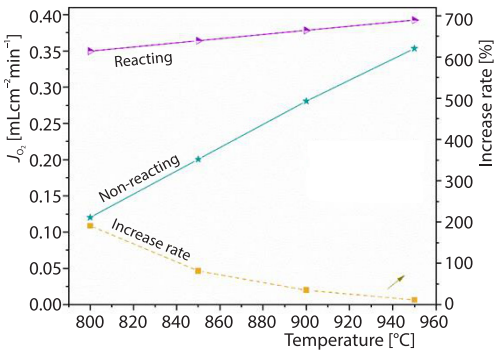

Figure 8. Variation of oxygen permeability with temperature under reactive and non-reactive conditions

The geometry of the permeation device (the gap height between the inlet and the membrane, the distribution of the gas inlet and the diameter of the inner tube*, etc.*) has a certain

influence on the oxygen permeability and reaction rate. In order to analyze the influence and causes of geometric shape, this section takes the gap height as an example for simulation analysis. Since the air inlet only affects the distribution of oxygen partial pressure on the feed side, the influence of the gap height between the air inlet and the membrane on the oxygen permeability under non-reaction conditions at 950 °C of the heat source temperature was studied. The results in fig. 9 show that the gap height between the air inlet and the membrane has little effect on the overall oxygen permeability, and the values are basically maintained at 0.337-0.353 mL/cm^{2}min at four gap heights of 0.5 mm, 1 mm, 2 mm, 3 mm, and 4 mm. When the gap height is less than 3 mm, the oxygen permeability increases with the increase of gap height, but when the gap height is more than 3 mm, the oxygen permeability changes oppositely. This may be due to the larger gap height makes the inlet fluid throat area larger, resulting in smaller flow velocity and lower oxygen partial pressure. However, the small gap height causes the flow velocity to increase, but the coating area of the jet fluid decreases, which is only limited to the high oxygen concentration in the membrane center region corresponding to the inlet. Therefore, two factors need to be considered in determining the gap height between the inlet and the membrane of the feed side. One is the fluid-flow rate, and the other is the coverage area of the fluid jet. Only when the two factors reach the trade-off can the oxygen concentration distribution be optimized.

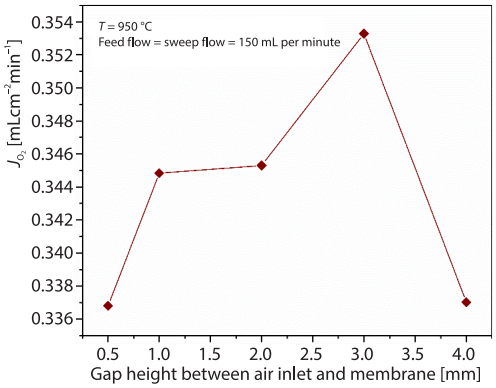

Figure 9. Effect of gap height between air inlet and membrane on oxygen permeability

The gap height between the sweeping inlet and the membrane has a great influence on the combustion reaction. Figure 10 shows the influence of the gap height on oxygen permeability. The results show that the oxygen permeability increases first and then decreases with the increase of gap height. When the gap is 3 mm, the oxygen permeability reaches the maximum. The reason for this rule is still that there are two trade-off factors that affect the oxygen permeability of the permeable side under reaction conditions, namely the momentum effect caused by the fluid inlet velocity and the temperature produced by combustion. When the gap increases from 1 mm to 3 mm, the increase of the gap height also leads to a larger throat area, resulting in a lower fluid-flow rate. At the same time, the combustion reaction is improved due to the longer contact time between fuel and oxygen, which promotes the combustion temperature, so the oxygen permeability increases. From the aforementioned analysis, it can be seen that in the range of low gap height, the combustion temperature plays a leading role in the oxygen permeability under the reaction conditions. On the contrary, when the gap height changes from 3-5 mm, the oxygen consumption is delayed due to the further decrease of the fluid-flow rate,

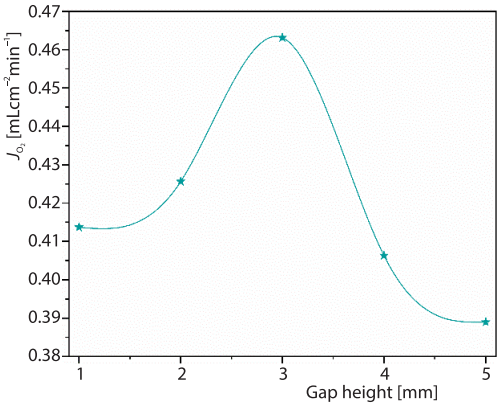

Figure 10. Effect of gap height between sweeping inlet and membrane on oxygen permeability

which leads to the increase of the oxygen partial pressure near the membrane on permeation side. This result further affects the reaction rate and combustion temperature, and aggravates the decrease of the oxygen permeability. At this time, the momentum effect caused by the flow rate plays a leading role in the oxygen permeability under the reaction conditions.

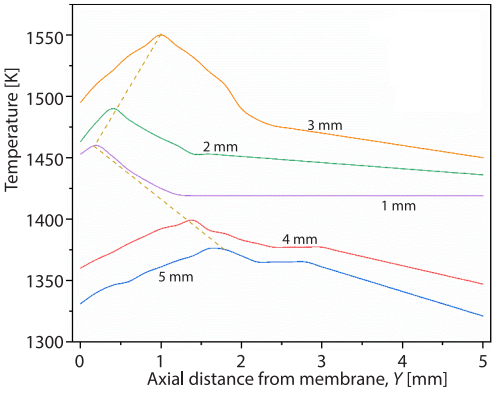

Figure 11. The variation of temperature with axial position under different gap height

The previous behavior changes are also reflected in reflected in the temperature change, fig. 11. When the is less than 3 mm, the temperature increases with the increase of the gap height. When the gap is more than 3 mm, the temperature decreases with the increase of the gap height. The overall change of temperature is consistent with the oxygen permeability. The overall combustion temperature is low, which is related to the low oxygen permeability of the dual-phase OTM. In the combustion promotion process of the single-phase perovskite membrane with high oxygen permeability, the corresponding change rule is expected to be more obvious. It is worth noting that the high temperature flame is suspended in the air-flow between the inlet and the membrane surface, and is located at the vertical distance of 0.2-1.6 mm. The flame position is mainly related to three factors: inlet gas velocity, oxygen permeability and CH_4 concentration. An increase in the gap height leads to a decrease in the inlet gas velocity, which leads to a flame position away from the membrane surface. The coordination of oxygen permeability and CH_4 concentration jointly determines the flame position, which is related to the optimal stoichiometric ratio of CH_4 to oxygen. Lower CH_4 concentrations make the effect of oxygen permeation insignificant at high gap heights, making the inlet gas velocity the determining factor for combustion flame position. Part of the thermal combustion gas recirculates around the corner area around the outer tube membrane, resulting in a corresponding increase in temperature and heat transfer rate in the area. The external re-circulation zone helps to stabilize the flame. The flame away from the membrane surface will also reduce the temperature of formed external re-circulation zone. From another point of view, the ceramic-based OTM is prone to thermal fracture when the temperature exceeds 1400 K. The effective cooling around the membrane area helps to control the membrane surface temperature and prevent thermal damage. The formation of the low velocity zone near the membrane leads to the flame away from the membrane surface, thus protecting it from the influence of thermal stress.

Conclusions

To explore the effects of hydrodynamic conditions and combustion reactions on oxygen transport, this paper innovatively combines the oxygen permeation model applicable to SDC-SSAF type dual-phase OTM with CFD to construct a 3-D model of the dual-phase membrane oxygen permeation process. At the same time, the distribution of concentration field and temperature field between different watershed areas is fed back intuitively. The accuracy of the model was proved by experimental validation.

The analysis of the calculation results shows that the inlet gas velocity shows a certain expansion angle, the oxygen concentration in the vicinity of the membrane shows a laminar decreasing trend. The oxygen concentrations on both sides near the membrane are 0.2275 and 0.0269, respectively, and there is an accumulation of oxygen at the corners around the perme-

able side. The growth of oxygen permeability slows down after the pressurization value on the feed side exceeds 30 kPa. The growth rate of oxygen permeability increased from 69.85-270.94% when the evacuation pressure increased from 10 kPa to 90 kPa after increasing the sweeping condition. The oxygen permeability increased by 0.356 mL/cm^{2}min at 950 °C when the oxygen concentration increased from 0.06 to 0.82. Combustion reaction increases oxygen permeability by 190.92% at 800 °C. The optimal selection of the gap between the gas inlet and the membrane should take into account various trade-offs such as the momentum effect caused by flow rate, the combustion rate and temperature, and gas injection area. The optimal gap height after trade-off in the model is 3 mm.

Acknowledgment

This work is financed by the National Key Research and Development Program of China under Grant No. 2018YFC0810001 and No.2017YFC0210303.

Nomenclature

A – pre-exponential factor
A_{cell} – area of grid cells, [m^2]
$D_{i,m}$ – diffusion coefficient
E_a – activation energy, [Jmol^{-1}]
J_{O_2} – oxygen permeability, [mLcm^{-2}min^{-1}]
P_o – reference pressure, [bar]
p – static pressure, [Pa]
R – universal gas constant, 8.314, [Jmol^{-1}K^{-1}]
r – area specific resistance, [Ωm^2]
S_h – source term
T – thermodynamic temperature, [K]
U_j – velocity vector, [ms^{-1}]
V_{cell} – volume of grid cells, [m^3]

Greek symbols

μ – dynamic viscosity, [Pa·s]
$\Delta\mu_{O_2}$ – chemical potential difference, [Jmol^{-1}]

Subscripts

o – standard atmospheric pressure
i – components

Superscripts

b – temperature index
I – peed side
II – permeation side

Acronyms

UDF – user defined functions
OTM – oxygen transport membrane

References

[1] Shao, Z. P., *et al*., A High-Performance Cathode for the Next Generation of Solid-Oxide Fuel Cells, *Nature*, *431* (2004), Sept., pp. 170-173
[2] Elbadawi, A. H., *et al*., Partial Oxidation of Methane to Syngas in Catalytic Membrane Reactor: Role of Catalyst Oxygen Vacancies, *Chemical Engineering Journal*, *392* (2020), 123739
[3] Bai, W., *et al*., A Comprehensive Review on Oxygen Transport Membranes: Development History, Current Status, and Future Directions, *International Journal of Hydrogen Energy*, *46* (2021), 73, pp. 36257-36290
[4] Zhang, Z., *et al.*, Highly Efficient Preparation of $Ce_{0.8}Sm_{0.2}O_{2-\delta}$-$SrCo_{0.9}Nb_{0.1}O_{3-\delta}$ Dual-Phase four-Channel Hollow Fiber Membrane Via One-Step Thermal Processing Approach, *Journal of Membrane Science*, *620* (2021), 118752
[5] Chen, G., *et a*l., Novel CO_2-Tolerant Dual-Phase Ce0.9Pr0.1O2-δ-La0.5Sr0.5Fe0.9Cu0.1O3-δ Membranes with High Oxygen Permeability, *Journal of Membrane Science*, *595* (2020), 117530
[6] Gu, Y., *et al*., Design and Simulation of Hybrid Thermal Energy Storage Control for Photovoltaic Fuel Cell, *Thermal Science*, *24* (2020), 5B, pp. 3259-3267
[7] Tikiz, I., *et al.*, An Experimental Investigation of Solid Oxide Fuel Cell Performance at Variable Operating Conditions, *Thermal Science*, *20* (2016), 5, pp. 1421-1433
[8] Cai, L., *et al.*, Effect of Ru and Ni Nanocatalysts on Water Splitting and Hydrogen Oxidation Reactions in Oxygen-Permeable Membrane Reactors, *Journal of Membrane Science*, *599* (2020), 117702
[9] Cheng, H., *et al*., Effects of B-Site Oped Elements in the Electronic-Conducting Perovskite Phase on the Property of Dual-Phase Membranes, *International Journal of Applied Ceramic Technology*, *14* (2017), 4, pp. 611-622

[10] Widenmeyer, M., *et a*l., Weidenkaff, Engineering of Oxygen Pathways for Better Oxygen Permeability in Cr-Substituted $Ba_2In_2O_5$ Membranes, *Journal of Membrane Science*, *595* (2020), 117558
[11] Behrouzifar, A., *et al*., Experimental Investigation and Mathematical Modelling of Oxygen Permeation through Dense $Ba_{0.5}Sr_{0.5}Co_{0.8}Fe_{0.2}O_3$-(BSCF) perovskite-type ceramic membranes, *Ceramics International*, *38* (2012), 6, pp. 4797-4811
[12] Guironnet, L., *et al*., The Surface Roughness Effect on Electrochemical Properties of $La_{0.5}Sr_{0.5}Fe_{0.}7Ga_{0.3}O_{3-\delta}$ Perovskite for Oxygen Transport Membranes, *Journal of Membrane Science*, *588* (2019), 117199
[13] Zhu, X., *et a*l., $Ce_{0.85}Sm_{0.15}O_{1.925}$-$Sm_{0.6}Sr_{0.4}Al_{0.3}Fe_{0.7}O_3$ Dual-Phase Membranes: One-Pot Synthesis and Stability in a CO_2 Atmosphere, *Solid State Ionics*, *253* (2013), Dec., pp. 57-63
[14] Wang, Z., *et al.*, A Novel Cobalt-Free CO_2-Stable Perovskite-Type Oxygen Permeable Membrane, *Journal of Membrane Science*, *573* (2019), Mar., pp. 504-510
[15] Shi, L., *et al*., High CO_2-Tolerance Oxygen Permeation Dual-Phase Membranes $Ce_{0.9}Pr_{0.1}O_{2-\delta}$-$Pr_{0.6}Sr_{0.4}Fe_{0.8}Al_{0.2}O_{3-\delta}$, *Journal of Alloys and Compounds*, *80*6 (2019), Oct., pp. 500-509
[16] Qiu, K., *et al*., Fluorine-Doped Barium Cobaltite Perovskite Membrane for Oxygen Separation and Syngas Production, *Ceramics International*, *46* (2020), 17, pp. 27469-27475
[17] Chae, J. W., *et al.*, Oxygen Permeation Properties of Sm/Sr Co-Doped Ceria Decorated $Ba_{0.5}Sr_{0.5}Co_{0.8}Fe_{0.2}O_{3-\delta}$ Hollow Fiber Membrane, *Journal oF Industrial and Engineering Chemistry*, *76* (2019), Aug., pp. 508-514
[18] Zangana, L. M. K., *et al*., Experimental Study and CFD Analysis of Energy Separation in a Counter Flow Vortex Tube, *Thermal Science*, *25* (2021), 1A, pp. 279-291
[19] Habib, M. A., *et al*., Nemit-Allah, Modelling of Oxygen Permeation through a LSCF Ion Transport Membrane, *Comput Fluids*, *7*6 (2013), May, pp. 1-10
[20] Feng, B., *et al*., The CFD Modelling of the Perovskite Hollow Fiber Membrane Modules for Oxygen Separation, *Chemical Engineering Science*, *230* (2021), 116214
[21] Nemitallah, M. A, *et al*., A Study of Methane Oxy-Combustion Characteristics Inside a Modified Design Button-Cell Membrane Reactor Utilizing a Modified Oxygen Permeation Model for Reacting Flows, *Journal of Natural Gas Science and Engineering*, *28* (2016), Jan., pp. 61-73
[22] Nemitallah, M. A., *et al*., Experimental and Numerical Study of Oxygen Separation and Oxy-Combustion Characteristics Inside a Button-Cell LNO-ITM Reactor, *Energy*, *84* (2015), May, pp. 600-611
[23] Nemitallah, M. A., *et al*., Design of an Ion Transport Membrane Reactor for Gas Turbine Combustion Application, *Journal of Membrane Science*, *450* (2014), Jan., pp. 60-71
[24] Ahmed, P., *et al*., Investigation of Oxygen Permeation through Disc-Shaped BSCF Ion Transport Membrane under Reactive Conditions, *International Journal oF Energy Research*, *41* (2017), May, pp. 1049-1062
[25] Nemitallah, M. A., *et al*., A Study of Methane Oxy-Combustion Characteristics Inside a Modified Design Button-Cell Membrane Reactor Utilizing a Modified Oxygen Permeation Model for Reacting Flows, *Journal of Natural Gas Science and Engineering*, *28* (2016), Jan., pp. 61-73
[26] Zhu, X., *et al.*, Permeation Model and Experimental Investigation of Mixed Conducting Membranes, *Aiche Journal*, *58* (2012), 6, pp. 1744-1754
[27] Shin, D., *et al.*, Optimization of an Ion Transport Membrane Reactor System for Syngas Production, *Energy Reports*, *8* (2022), Nov., pp. 3767-3779
[28] Li, C., *et al.*, Rate Determining Step in SDC-SSAF Dual-Phase Oxygen Permeation Membrane, *Journal of Membrane Science*, *573* (2019), Mar., pp. 628-638
[29] Catalan-Martinez, D., *et al*., Characterization of Oxygen Transport Phenomena on BSCF Membranes Assisted by Fluid Dynamic Simulations Including Surface Exchange, *Chemical Engineering Journal*, *387* (2020), 124069
[30] Li, C., *et al*., Oxygen Permeation through Single-Phase Perovskite Membrane: Modelling Study and Comparison with the Dual-Phase Membrane, *Separation and Purification Technology*, *235* (2020), 116224
[31] Mastropasqua, L., *et al*., Simulation of Oxygen Transport Membranes for CPO Reactors in Small-Scale Hydrogen or Syngas Production Applications, *Energy Procedia*, *142* (2017), Dec., pp. 1589-1594
[32] Hong, J., *et al*., Interactions between Oxygen Permeation and Homogeneous-Phase Fuel Conversion on the Sweep Side of an Ion Transport Membrane, *Journal of Membrane Science*, *428* (2013), Feb., pp. 309-322

Paper submitted: June 25, 2022
Paper revised: October 31, 2022
Paper accepted: November 15, 2022